Effect of thickness on photoconversion efficiency of Al$_2$TiO$_5$/TiO$_2$/Al$_2$O$_3$ nanocomposite films as photoanodes in water splitting

Shima Kashani [1], Hamid Reza Madaah Hosseini [2,3,*]

[1]Materials Science & Engineering Department, Sharif University of Technology, International Campus, Kish Island, Iran;
[2]Materials Science and Engineering Department, Sharif University of Technology, Tehran, Iran;
[3]Institute for Convergence Science and Technologies, Sharif University of Technology, Tehran, Iran.

ABSTRACT

The thickness of the photoanode film plays a crucial role in the photoelectrochemical (PEC) water splitting process, significantly impacting the photoconversion efficiency. The optimal thickness of the photoanode enhances the photocurrent density by making a balance between light absorption and electrolyte mass transfer. The main goal of this study was to investigate the effect of thickness on the photoelectrochemical performance of the Al$_2$TiO$_5$-based nanocomposite layer as a photoanode under the sunlight simulator. Al$_2$TiO$_5$/TiO$_2$/Al$_2$O$_3$ nanocomposite was initially synthesized utilizing the citrate sol-gel technique, and after the calcination at 800°C, it was deposited on the fluorine-doped tin oxide coated glass slide (FTO) substrate by the doctor blade method in which, several films of various thicknesses can be prepared from a unique paste, by just changing the adhesive tape layers. The Diffuse Reflectance spectroscopy (DRS) technique was utilized to determine the band gap energy value of all specimens, and the field emission scanning electron microscopy (FE-SEM) method was used to investigate the morphology and to determine the thickness of the deposited films. The X-ray diffraction (XRD) analysis exhibited the presence of the tialite (Al$_2$TiO$_5$) phase besides the anatase, rutile, and corundum phases. The cyclic voltammetry (CV) measurements were utilized to estimate the accessible surface area in specimens. Different photoelectrochemical results were expected to be obtained by the photoanodes with different thicknesses of the Al$_2$TiO$_5$/TiO$_2$/Al$_2$O$_3$ nanocomposite films. Photoelectrochemical (PEC) measurements revealed that the highest photoconversion efficiency was achievable by the tialite-based sample by the thickness of about 5 µm which was about 20% higher than the obtained value by the thinner or even thicker tialite-based nanocomposite samples.

Keywords: *Aluminum titanate, Photoconversion efficiency, Thickness, Sol-gel.*

1. Introduction

Photoelectrochemical (PEC) water splitting has attracted considerable interest as the "holy grail" for solar energy conversion and storage. However, most semiconductor photoanodes studied for PEC water splitting face numerous challenges. Two main concerns are the insufficient generation of photogenerated charge carriers and the slow kinetics of water oxidation, leading to rapid recombination of charges at both the bulk and surface levels. Additionally, the relatively wide band gap imposes limitations on improvements in solar energy conversion efficiency. Nanostructured photoelectrodes offer significant benefits such as improved light dispersion, large surface area, enhanced charge transfer, and shortened carrier diffusion pathways. These attributes facilitate enhanced light absorption, efficient charge carrier transport, and increased efficiency in redox reactions. However, while large surface areas and nanostructures

bring advantages, they can also introduce challenges, such as heightened surface recombination and a decrease in the thickness of the space charge layer. These factors may hinder effective charge separation and transport [1]. The minority charge carrier diffusion length plays a critical role in determining charge carrier transfer efficiency. Unfortunately, due to the high recombination rate in many photocatalysts, the minority carrier diffusion length is very short. For example, while TiO_2 has a hole diffusion length ranging from 10 to 100 nm [2], Fe_2O_3 exhibits a much shorter range of 2 to 4 nm [3]. Short diffusion lengths are linked to high recombination rates, which in turn reduce charge separation and transportation efficiency. Moreover, short diffusion lengths impose limitations on the thickness of the absorption layer, resulting in decreased light absorption efficiency. Due to the significant effect of thickness on PEC water splitting performance in TiO_2 thin films, several deposition techniques that allow controlling the thickness of the TiO_2 layer on FTO substrate with good uniformity, such as the electrophoretic deposition (EPD) technique [4] paste coating [5], spin coating [6], and sputter deposition [7] were utilized. Nanocrystalline TiO_2 thick films deposited by the EPD technique on FTO glass with a thickness of 14.6 µm exhibited the highest photoconversion efficiency of 2.49% [4]. The maximum photocurrent efficiencies had a linear dependency on the thickness of the oxide layer in Ti/TiO_2 heterostructure thick films. For the thinnest coating layer (4 µm), the efficiency of nearly five times larger than the thickest photoanode was obtained, while better electrical contact of the thinnest oxide layer to the substrate was known as the reason for this manner [4]. Despite its popularity in photocatalytic studies, as a metal oxide (MO) semiconductor, TiO_2 faces drawbacks that hinder its efficiency as a photo-anode (PA) for PEC water splitting. Notably, its relatively large band gap restricts absorbance to a narrow UV wavelength range, comprising only about 5% of the solar spectrum [8]. To broaden sunlight absorption, numerous composites, such as SnO_2/TiO_2, ZnO/TiO_2, Cu_2O/TiO_2, Al_2O_3/TiO_2, and others, have been synthesized in which, establishing the internal electric field at the interface of the MO/MO junction, leads to the minimization of charge carrier recombination, and facilitating effective charge transfer within the active layer, in photo-anodes (PAs) [9-12]. The TiO_2 tubular structure, incorporating sub-stoichiometric Ti-O phases within the composite, demonstrated a 2.5-fold enhancement in photocurrent density at 1.23 V vs. RHE and a 2.8-fold rise in photoconversion efficiency achieved at a lower bias compared to the pristine TiO_2. The photocurrent density achieved by the SnO_2/TiO_2 composite-based photoanode reached 0.89 mA cm^{-2}, which was about nine times higher than the measured value in the case of bare TiO_2 photoanode [9]. The overpotential for TiO_2/SnO_2 nanocomposite was about 570 mv [13]. $Al_2TiO_5/TiO_2/Al_2O_3$ nanocomposite mixtures as a photocatalyst material were first investigated by F.Bakhshandeh et al. It was shown that the methylene blue (MB) photodegradation of these composites is much more than nanostructured anatase [14]. Later, Al_2TiO_5-based nanocomposites have also been investigated as highly photoactive materials in research [15-17]. Heterostructure Al_2TiO_5/TiO_2 catalyst due to the reduced band gap and more hydroxyl groups formed on the surface exhibited higher photocatalytic activity than that achieved by pristine TiO_2 or by the Al_2TiO_5 (AT) under UV irradiation [18], while presence of oxygen vacancy inside this heterostructure was reported as an important parameter in the PEC performance enhancement of Al_2TiO_5/TiO_2 layers [19].The sol-gel process allows for precise control over the composition, homogeneity, purity, and microstructure of the final product. It is a low-temperature, low-cost technique widely used in the production of ceramics, glasses, and nanomaterials. This method offers precise control over the morphology and crystallinity of synthesized photoelectrodes, which is crucial for optimizing their performance [20-22]. However, the sol-gel method's effectiveness is highly dependent on the solvents and precursors used, which can impact the quality and consistency of the synthesized photoelectrodes [23]. Significant efforts have been made to synthesize aluminum titanate (AT) nanoparticles using low-temperature methods, eliminating the need for prolonged high-temperature sintering of oxide compounds like Al_2O_3 and TiO_2. AT nanoparticles were produced by Sobhani et al. via a sol-gel process using aluminum chloride and titanium tetrabutoxide (TTIP), resulting in an average particle size under 100 nm, though the nanoparticles tended to agglomerate into a cabbage-like shape [24]. Andrianainarivelo et al. synthesized Al_2TiO_5 at low temperatures, above 600 °C, without forming TiO_2 or $Al2O_3$ phases using a non-hydrolytic sol-gel procedure [25]. Azarnia et al. used the citrate sol-gel method to synthesize aluminum
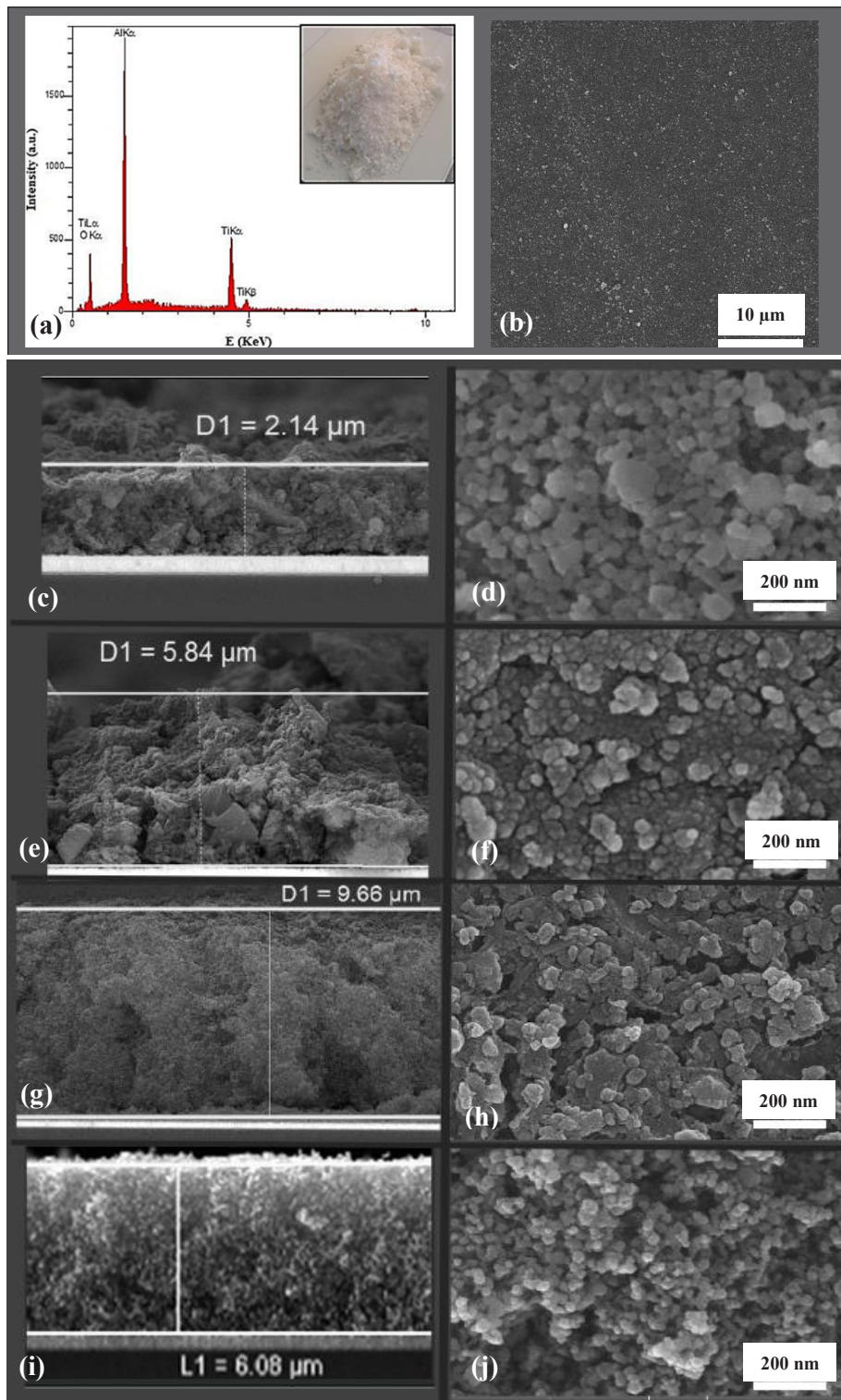
Fig. 1- SEDX analysis (a) and FE-SEM image (b) of the AT-based nanocomposite powder. The inset image shows a picture of the AT-based nanocomposite powder. FE-SEM images of the cross-sectional view and top view for the AT2 sample (c) and (d), the AT5 sample (e) and (f), the AT9 sample (g) and (h), and the P25 sample (i) and (j).

titanate (AT) nanostructured powder, achieving grain sizes smaller than 70 nm [26]. In the present work, novel photoactive nanocomposite materials comprising $Al_2O_3/TiO_2/Al_2TiO_5$ were used as photoanodes for water splitting. The primary objective is to examine how thickness affects the PEC performance of these electrodes. Since thickness is the sole variable parameter in this study, all samples were produced from a single batch of powder, prepared using a specific process, and maintained at a consistent temperature. The layer thickness was controlled using an adjustable deposition technique." The morphological, structural, and optical properties of AT-based nanocomposite layers with various thicknesses deposited on FTO substrates were studied. The authors aimed to optimize the thickness to achieve the maximum photocurrent density in the processed composite films.

2. Experimental
2.1. Materials and preparation of AT-based nanocomposites

Tialite nanoparticles were synthesized through a sol-gel approach using aluminum chloride ($AlCl_3$), citric acid ($C_6H_8O_7$), anhydrous titanium isopropoxide (TTIP, C16H36O4Ti), and absolute ethanol (C_2H_6O) as precursors, all acquired from Merck Company. The synthesis process, mechanism of microstructural evolution, and phase transformation of nanostructured aluminum titanate (Al_2TiO_5) particles have been detailed extensively in the literature. [14, 26, 27]. Synthesis: In a nitrogen (N_2) gas environment, 4 g of $AlCl_3$ powder dissolved completely in 35 ml of ethanol, followed by the gradual addition of TTIP to the solution using a standard syringe under stirring at room temperature. Subsequently, 1.5 g of anhydrous citric acid was added, and the solution was stirred for 15 minutes. The preparation process was carried out in a sealed chamber to minimize the impact of oxygen or humidity on the bonding between Al and Ti ions during gelation. This led to the formation of a homogeneous, honey-colored solution, which underwent reflux at 80 °C for 1 hour. Following reflux, a colorless gel with high homogeneity and transparency was obtained. The synthesized gels were dried at 100 °C for 24 hours in an oven and then ground. The resulting powder underwent calcination at 800 °C for 2 hours.
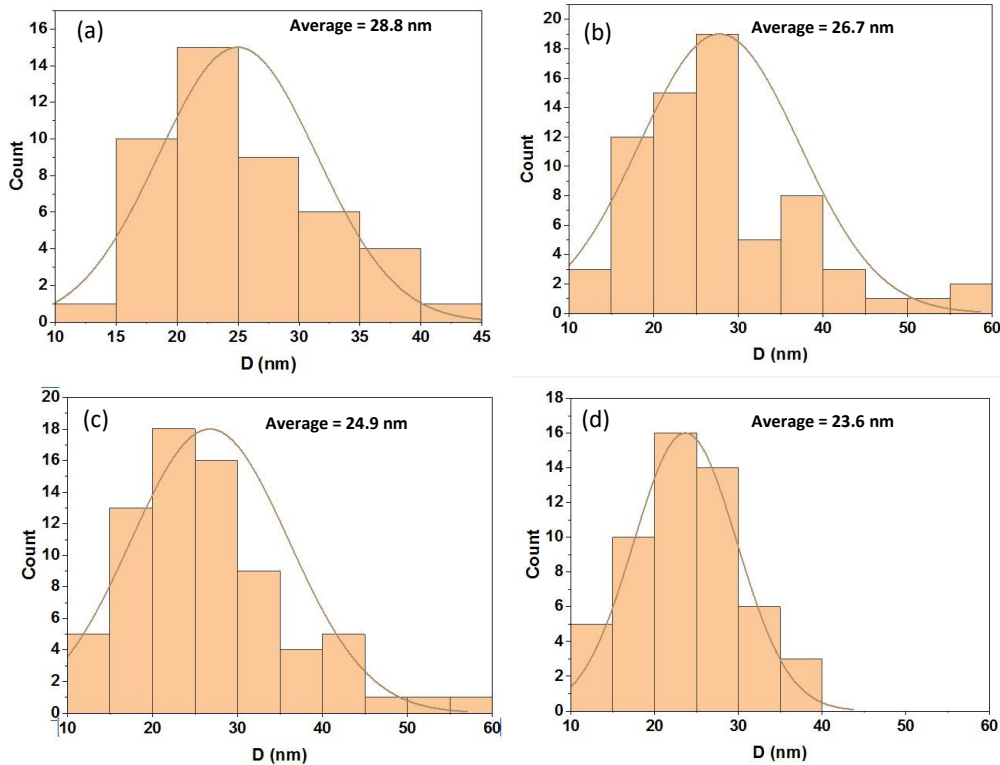

Fig. 2- Size distribution for AT2 sample (a), AT5 sample (b), AT9 sample (c) and P25 sample (d).

2.2. Fabrication of AT-based nanocomposite electrodes

The combination of high conductivity, optical transparency, chemical stability, nanostructured scaffold capability, cost-effectiveness, and compatibility with photoactive materials makes fluorine-doped tin oxide (FTO) glass an ideal choice of substrate for constructing efficient photoelectrodes for water splitting applications [28, 29].

2.2.1. Substrate Preparation

The glass slide substrates (FTO) were prepared using common pre-treatment methods [30, 31]. The initial step was cleaning. The FTO sheets were sequentially washed with a soap solution, acetone, and then ethanol to remove surface contaminants like carbon. The next step was acid treatment to remove surface contaminations and improve the surface roughness of these sheets. This involved immersing the slides in a solvent of 0.1 M hydrochloric acid in ethanol and sonication for 15 minutes in an ultrasonic bath. After each step, the glass slide substrates were rinsed with deionized (DI) water. Finally, after depositing a compact TiO_2 blocking layer, the FTO substrates were annealed at 350 °C for 30 minutes.

2.2.2. Blocking Layer Deposition

An acidic solution of titanium isopropoxide in ethanol was used to deposit a dense layer of TiO2 nanoparticles (5-10 nm) as a blocking layer. Two solutions were prepared according to the specified formula, and the second solution was incrementally added drop by drop to the first one while being stirred on a stirrer.
1. TTIP (369 μl) + Ethanol (2.53 ml)
2. HCl (35μl) + Ethanol (2.53 ml)

Subsequently, the prepared solution was drop-cast onto the FTO substrate at a spinning rate of 2000 rot.min⁻¹ for 30 seconds. Powders of Commercial TiO_2 (P25 Degussa), Al_2O_3, AT-based nanocomposite, and cellulose powder were introduced into ethanol within a glass vial to formulate pastes. Ethyl cellulose was dispersed as each powder was added to the solution on a magnetic stirrer. The resulting pastes were then applied to FTO substrates using the " doctor blade method," [32,33] followed by annealing the samples at 450 °C for 30 minutes. Then, to create samples with greater thickness and ensure accurate coating, the doctor blade in series method was used [34]. The samples that were coated once using the doctor blade method were named AT2, while the subsequent samples prepared using the doctor blade in the series method were named AT5 and AT9. A paste made from powders of commercial TiO_2 (P25 Degussa) was also prepared in a manner identical to the composite sample. This paste was then coated onto the FTO substrate using the doctor blade method. In this study, this sample is referred to as P25.

2.3. Characterization

Surface morphology and the EDX analyses of all AT nanocomposite thick films were investigated using Field emission scanning electron (FE-SEM) microscopy Philips Model XL30, Netherlands. To identify the crystalline composition of the nanocomposite photoanodes, the X-ray diffraction (XRD) pattern was recorded utilizing a Netherland / PW3710 / PHILIPS. The Scherrer equation (Eq. 1) was used to calculate the average crystallite size of samples [35]:

$$D = \frac{0.9\,\lambda}{\beta \cos\theta} \tag{1}$$

In this equation, λ represents the X-ray wavelength, θ is defined as the diffraction angle of the peak (in degrees), and β is the full-width at half-maximum (FWHM).

DRS analysis utilizing an Avaspec-2048-TEC instrument was conducted to assess the diffuse reflectance and determine the optical band gap value for the specimens. To determine the band gap energy of the samples using the provided data, one may proceed with the following steps:

(i) Estimating F(R) utilizing the Kubelka-Munk function is done as follows [36]:

$$F(R) = \frac{(1-R)^2}{2R} \tag{2}$$

(ii) In the Tauc method, the conversion of F(R) to the energy involves using the term of $[F(R)h\nu]^n$. In electronic transitions, the value of (n) is assigned differently: (n = 0.5) for the indirect transition, and (n = 2) for a direct transition. In this context, (h) denotes Planck's constant (J·s), and (ν) represents the frequency of light (s⁻¹). The subsequent procedure entails generating the Tauc plot to assess the values of the optical band gap energy (E_g). This process involves plotting the term $[F(R)h\nu]^n$ against energy in eV and extracting E_g values by linearly extrapolating the linear segment of the curve [36].

The cyclic voltammetry (CV) analysis was conducted using an Autolab potentiostat/galvanostat

electrochemical workstation (PGSTAT302N, The Netherlands) in a three-electrode configuration with 1M saturated NaOH electrolyte at room temperature. Scan rates ranging from 10 to 80 mV/s were employed. PEC performance of AT-based nanocomposite layers deposited on FTO compared with P25 on thick film FTO was measured using a traditional three-electrode system in 1M NaOH electrolyte (PH≈13.6). The photocurrent density measurements over a range of the applied potential (J–V) scans were accomplished under the simulated solar light AM 1.5 G at 100 mW/cm².

3. Results and discussion

Micrographs of cross-sectional and top views of AT-based thick film electrodes with different thicknesses are displayed in Fig. 1. Cross-sectional

views of aluminum titanate-based nanocomposite films for AT2 specimens show that it has 2.14 μm thickness. The thickness of the AT5 specimen is 5.84 μm, while the AT9 specimen, being the thickest film, has a thickness of 9.66 μm. The P25 electrode, which consisted of a 6 μm layer of TiO_2 nanoparticles, was chosen as a reference for comparison with the optimized sample, AT5, in this research. The cross-sectional and top views of the P25 sample are also depicted in Fig. 1. The FE-SEM images, revealed partially spherical morphology of the $TiO_2/Al_2O_3/Al_2TiO_5$ nanocomposite thick films. There was a homogeneous nanostructure with some pores inside the layer, which allowed the penetration of electrolytes through the bulk. In this study, the ImageJ processing program was utilized to measure the size distribution of all samples.
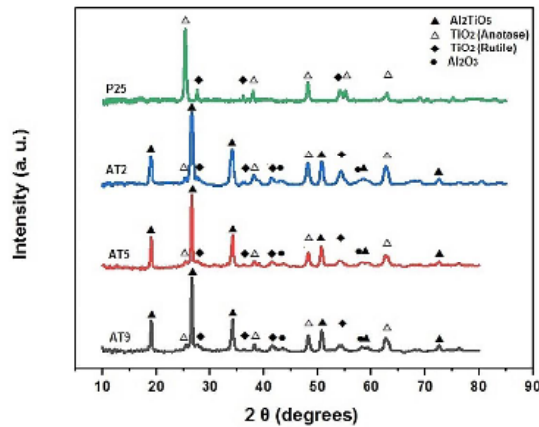

Fig. 3- X-ray diffraction patterns of (a) AT-based nanocomposite films and (b) P25 sample.
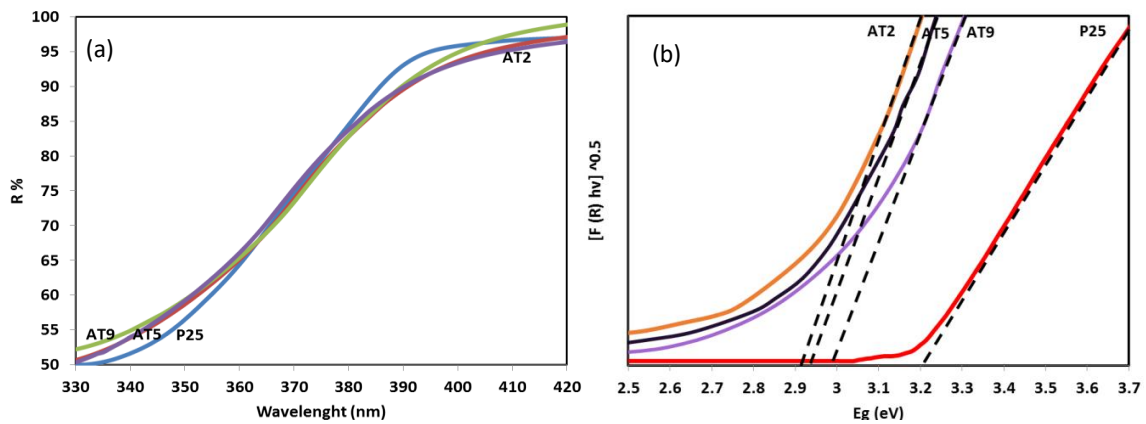

Fig. 4- (a) Diffuse reflectance spectroscopy plots (b) The Tauc plots of AT-based nanocomposites and P25 sample.

The size distribution was measured to be between 10 to 60 nm and size distributions of specimens are displayed in Fig. 2. Since all electrodes were prepared from a single paste, it was expected that the chemical composition of the surface would be consistent across all samples and that they would contain identical crystalline phases. EDX analysis data is depicted in Fig.1, indicating the presence of Ti, Al, and O elements without the presence of any impurities on the surface of photoanodes.

The XRD results for AT-based nanocomposite specimens are depicted in Fig. 3. District peaks were observed and according to the references were identified as anatase (TiO_2, tetragonal crystal structure, ICSD 98-000-5226), rutile (TiO_2, tetragonal crystal structure, ICSD 98-005-2025), and corundum (a-Al_2O_3, hexagonal crystal structure, ICSD 98-001-6920), phases beside a great deal of the tialite phase (Al_2TiO_5, orthorhombic crystal structure, ICSD 98-011-4495).

DRS measurement results for all the AT-based nanocomposites and the P25 photoelectrodes are depicted in Fig. 4 (a). The bandgap value (E_g) for the layers was determined by extrapolating the linear portion of Tauc's plot to its intersection with the hν-axis (Fig. 4(b)) [36].

The estimated bandgap energy (E_g) for photoelectrodes based on the Al_2TiO_5 phase, falls within the range of 2.92 eV to 2.97 eV, whereas the measured bandgap energy for the P25 sample was approximately 3.21 eV. Thickness, crystalline phase,

average crystallite size, average particle size and the band gap value of each sample are listed in Table. 1.

3.1. Photoelectrochemical measurements

The double-layer capacitance is affected by the specific surface area of the electrode, which determines the amount of charge that can be stored in the double layer. A larger surface area allows for more charge accumulation, leading to a higher capacitance. Therefore, as the electrochemical surface area thickness of the electrode increases, the double-layer capacitance also tends to increase. To compare the accessible surface area of the AT-based nanocomposites (AT2, AT5, AT9) and the P25 samples, the double-layer capacitance (C_{dl}) estimation via cyclic voltammetry (CV) measurement was used. The CV measurements were performed three times with a new working electrode for each iteration, indicating the excellent reproducibility of the prepared electrodes. The Electrochemically Active Surface Area (EASA) was estimated using the equation EASA = C_{dl}/C_s. During each scan, CV curves were obtained within a non-faradaic region (-0.3 to -0.2 V), where the anodic voltammetry scan proceeded with a positive sweep until it was reversed. The measurements were referenced to the Ag/AgCl potential. As depicted in Fig. 5, the curves exhibited a similar shape, resembling a standard electrochemical oxidation/reduction cycle curve.

By calculating the double-layer capacitance for the samples, the effective electrochemical active

Table 1- Thickness, band gap value, and the crystalline phases of AT-based nanocomposite and P25 film

Sample	Thickness (μm)	Crystalline phase	Average Crystallite size (nm)	Average particle size (nm)	E_g (eV)
AT2	2.18	Anatase Rutile Aluminum titanate Curundum	22.7	28.8	2.92 ± 0.02
AT5	5.84	Anatase Rutile Aluminum titanate Curundum	24.1	26.7	2.93 ± 0.02
AT9	9.66	Anatase Rutile Aluminum titanate Curundum	23.7	24.9	2.97 ± 0.01
P25	6.08	Anatase/Rutile	21.4	23.6	3.21 ± 0.01

surface area (EASA) was estimated [37]. Subsequently, the Double-Layer Capacitance (C_{dl}) was determined from the slope of the linear regression using the following formula [37]:

$$C_{dl} = \frac{m}{2A} \tag{3}$$

Where m is the slope of the linear regression, and *A* is the electrode surface area.

The estimated value of the double-layer capacitance for the AT2 sample is 91 mF, while this value for the AT5 and AT9 samples are 135 mF and 228 mF in sequence. The double-layer capacitance value for the P25 sample was measured to be 148 mF. C_s is a constant parameter representing the specific capacitance of standard electrode materials per unit surface area. However, for the $Al_2TiO_5/TiO_2/Al_2O_3$ nanocomposite, this value is unknown and not reported in the literature. Therefore, only the

double-layer capacitance (C_{dl}) was calculated for all samples, and the obtained values were used to compare the effective electrochemical active surface areas. As is seen, in Fig. 6 the AT9 sample exhibits the highest EASA value, whereas the AT2 sample has the minimum EASA.

3.2. The photocurrent measurements

The photocurrent under simulated sunlight indicates the photoelectrochemical (PEC) water oxidation reaction occurred at the surface of photoanodes. The photocurrent response curves are shown in Fig. 7. It can be seen from these plots that by increasing the applied bias potential, the photocurrent density increases until a saturated value are obtained.

It is worth mentioning that the minimum voltage required for the water splitting reaction to occur is 1.23 V. However, thermodynamic losses (approx-
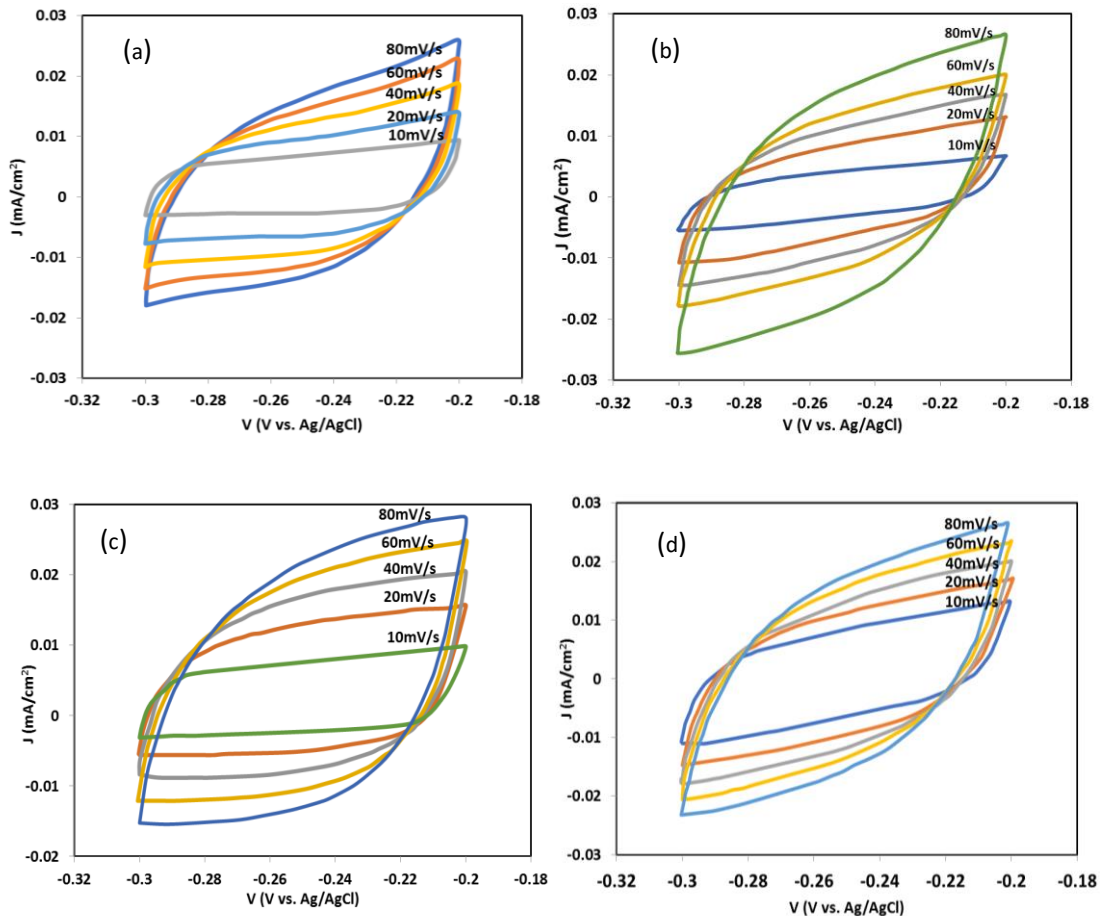

Fig. 5- Cyclic voltammograms performed in non-faradic region (-0.2 to -0.3 V vs. Ag/AgCl) at the scan rates of 10, 20, 40, 60, 80 (mV/s) for (a) AT2, (b) AT5, (c) AT9 and (d) P25 specimens.

imately 0.3–0.4 V) and overpotentials necessary for ensuring rapid reaction kinetics (about 0.4–0.6 V) elevate this value to around 1.9–2.2 V. [38]. In practice, by utilizing electrochemical impedance spectroscopy, the capacitance of the Schottky junction at the surface of the electrode can be found and is known as the flat band potential (U_{fb}). In reality, due to the required overpotential for the water oxidation reaction (η_{ox}), the photocurrent onset potential (V_{on}) is higher than the U_{fb}. When the applied bias is lower than the flat band potential of the interface between the electrode and the electrolyte ($V < U_{fb}$), due to the accumulation of the majority charge carriers (i.e., electrons for a photoanode) at the surface of the electrode, they are transferred to the electrolyte and compete with the oxidation process of water. When the applied bias compensates with the flat band potential ($V = U_{fb}$) there is no net current because there is a balance between the anodic and the cathodic reactions. The anodic photocurrent starts just when the applied bias is higher than the flat band potential. Then, the photogenerated charge carriers are transferred to the electrolyte under this bias and participate in water oxidation reactions. The magnitude of the overpotential is achievable from the difference between the onset potential and the flat band potential by using the following equation [38]:

$$\eta_{ox} = V_{on} - U_{fb} \qquad (4)$$

The photocurrent onset can be found by measuring the photocurrent density as a function of the applied bias and then comparing the illuminated and dark currents. In optimal conditions, the point at which the semiconductor shifts from ac-
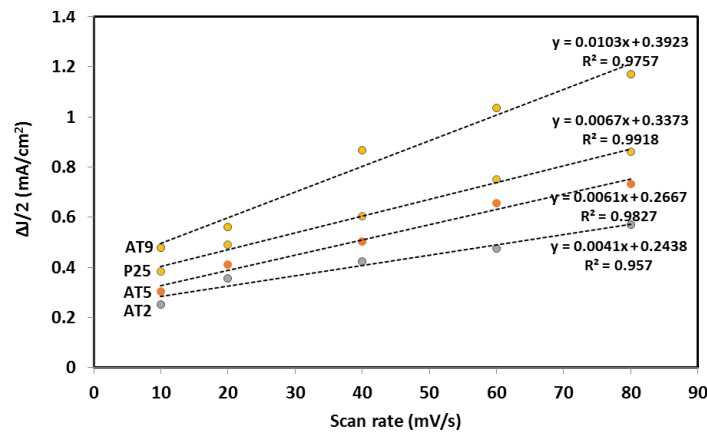

Fig. 6- A linear regression analysis conducted on the current density variances within the midrange of the potential window during cyclic voltammetry versus the scan rates for both the AT-based nanocomposites and the P25 specimens.
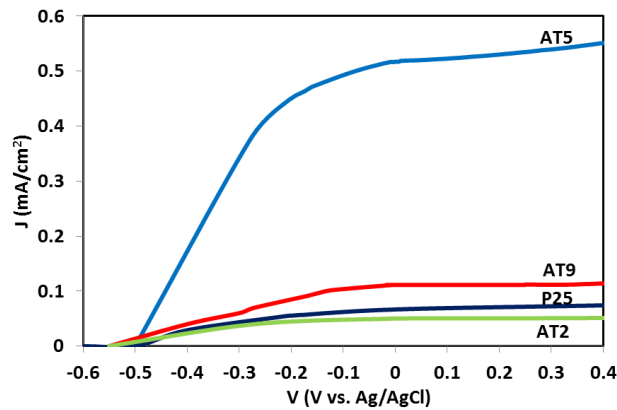

Fig. 7- Linear sweep voltammogram (LSV) measurements of AT-based nanocomposites and P25 photoelectrodes.

cumulation to depletion aligns with the initiation of photocurrent. This specific potential is defined as E_{fb}, yet it is frequently influenced by the kinetic overpotential essential for propelling the reaction forward. As the microstructure of the layer is influenced by the thickness of the layer, it determines how much absorption of light occurs in the film and the amount of photogenerated charge carriers reaching the surface of the electrode and participating in water oxidation reactions [39, 40]. Thinner layers reduce recombination through the bulk, while thicker layers enable deeper penetration and absorption of light, leading to the generation of a higher amount of electron-hole pairs through the

nanostructured material. It appears from Fig. 7 that the photocurrent onset is not affected significantly by the thickness of the layer, while the film thickness effect on photoresponse is visible. As seen in the plots, the photocurrent onset for AT2 and AT9 are observed at potential values of approximately -0.45 V, while these samples exhibited a comparatively lower saturated photocurrent density in comparison with other specimens. However, the relationship between thickness and photocurrent density is complex and may be influenced by other factors, such as the presence of different regions with varying degrees of orientation and the microstructure of the photoanodes. In this tradeoff, there

Table 2- Photoelectrochemical properties of AT-based and P25 photoanodes in 1M NaOH electrolyte

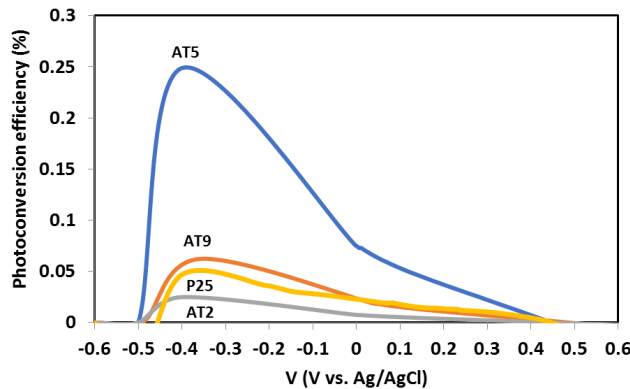| Sample	V_{onset} (V)	V_{fb} (V)	Overpotential (V)
AT5	0.52	0.18	0.34
P25	0.58	0.38	0.2

Fig. 8- Photoconversion efficiency curves as a function of the applied potential. The reported specimens are AT-based nanocomposite layers in comparison with the P25 electrode.
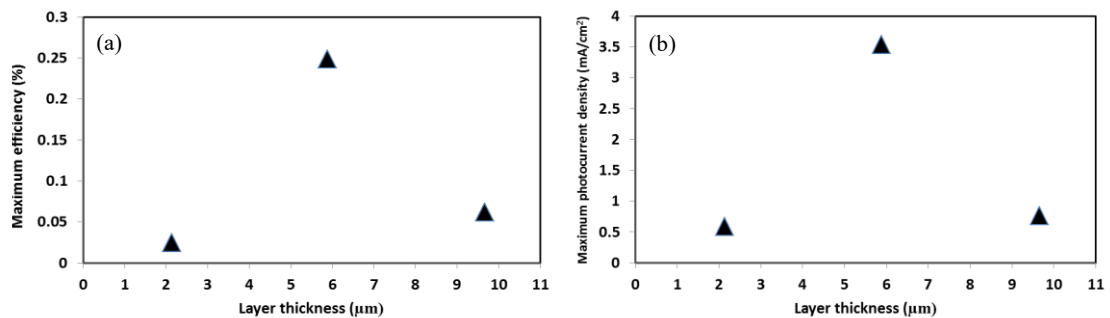

Fig. 9- (a) Maximum photoconversion efficiency and (b) maximum photocurrent as a function of the thick film layer thickness.

is an optimum thickness in which the photocurrent density reaches the highest value. It seems that in the case of the tialite-based photoanodes, the optimum for the thickness of the layer would be about 5 μm (AT5). The onset potential value for the AT5 sample was estimated to be 0.52 V. Then, due to the efficient charge carrier separation, under the applied bias, the photocurrent density exhibited a gradual increase with the increment of the applied bias. The highest obtained photocurrent density for the AT5 sample was 0.58 mA/cm2 at 0.4 $V_{Ag/AgCl}$ respectively. This result was confirmed by the higher photoconversion efficiency of this sample compared with other thick films of different thicknesses in this study. The onset potential, flat band potential, and overpotential for the AT5 sample, in comparison with the P25 sample as the reference electrode, are listed in Table 2.

The photoconversion efficiency (η) as a function of the applied bias for AT-based nanocomposites and P25 photoelectrodes was calculated using eq. 5 [41]:

$$\eta\ (\%) = J_p \times (2) \times [\ (E°_{rev} - |E_{app}|)/I_{light}]\times 100 \quad (5)$$

Where:
J_p is the photocurrent density (mA/cm^2)
I_{light} is the incident light irradiance
$E°_{rev}$ is the standard reversible potential (1.23 V $_{RHE}$)

E_{app} is the applied potential, calculated as E_{app} = E_{meas} - E_{aoc}, where E_{meas} represents the electrode potential (vs. Ag/AgCl) of the working electrode, and E_{aoc} is the electrode potential (vs. Ag/AgCl) of the same working electrode under open circuit condition and illumination.

The photoconversion efficiency curves (η(%)), obtained utilizing eq. 5 for the complete collection of thick films, are depicted in Fig. 8.

Photoconversion efficiency results indicate the strong effect of thickness on the photoelectrochemical performance of AT-based photoelectrodes. In Fig. 8, it's evident that sample AT5, with the highest achievable photocurrent densities, also demonstrates the highest photoconversion efficiency under an illumination intensity of 100 mW cm^{-2}. Specifically, this efficiency is five times greater than that observed for the TiO$_2$ P25 sample under identical conditions. The photocurrent densities of AT-based nanocomposite photoelectrodes at -0.4 $V_{Ag/AgCl}$ and the maximum photocurrent efficiencies of these samples are sketched as a function of the layer thickness in Fig.9.

In the case of tialite-based photoelectrodes, parameters affecting photoconversion efficiencies — such as band gap, particle size and morphology, and crystal structure—were carefully controlled during preparation. The thickness of the film, which determines the light absorption, strongly influences photoconversion efficiency which is limited by the diffusion length of minority carriers in semiconductor materials [42].In the case of this study, the tialite-based nanocomposite photoelectrodes with an average nanoparticle size of 25 nanometers, is approximately 5 micrometers (AT5 sample). These samples were prepared utilizing the sol-gel method, which allows for the formation of a homogeneous composite with controllable composition and microstructure. Their crystal structures were determined by the heat treatment, which was the same for all specimens resulting in a final product with a smaller energy band gap compared to titanium dioxide, leading to a higher photocurrent density in comparison with the P25 sample containing TiO$_2$ phase with an average particle size of 25 nm. Maximum values of the photoconversion efficiency and photocurrent density as a function of thickness for all specimens are shown in Fig. 9.

According to these results, the best performance is attributed to the AT5 by the maximum photoconversion efficiency of 0.25% at about -0.4 $V_{Ag/AgCl}$, which was even better than the measured value of the P25 sample as a reference for this study.

4. Conclusions

Al$_2$TiO$_5$/TiO$_2$/Al$_2$O$_3$ nanocomposite films of different thicknesses were prepared by sol-gel method and deposited on fluorine-doped thin oxide glass substrates. The estimated optical bandgap energy (E$_g$) using the Kubelka-Munk model in analyzing the DTS plots was about 2.9 eV for Al$_2$TiO$_5$/TiO$_2$/Al$_2$O$_3$ nanocomposite layers. The effect of thickness on the photoelectrochemical activity of Al$_2$TiO$_5$-based nanocomposite thick films was investigated under the sunlight simulator in aqueous 1M NaOH electrolyte, respectively and the following results were obtained.

1. All photoanodes were active under visible light illumination and promising for water splitting applications.

2. According to the results, morphology and crystal structures are similar in these samples, so the different photoelectrochemical activity of these samples is specifically related to their different sur-

face areas.

3. It was seen that the ability of semiconductor film to carry the electronic charges, was affected by the photoanode layer thickness significantly and eventually, the slightly different photoelectrochemical behavior was recorded by the samples.

4. The obtained photoconversion efficiency of the aluminum titanate-based sample with the optimum film thickness of about 5 μm under the illumination intensity of 100 mW cm^{-2} was five times higher than the resulted value for the TiO$_2$ P25 sample in the same situation at 0.6 V vs. RHE.

References

1. Seiß V, Helbig U, Lösel R, Eichelbaum M. Investigating and correlating photoelectrochemical, photocatalytic, and antimicrobial properties of TiO$_2$ nanolayers. Scientific Reports. 2021 Nov 12;11(1):22200.
2. Salvador P. Hole diffusion length in n-TiO$_2$ single crystals and sintered electrodes: Photoelectrochemical determination and comparative analysis. Journal of applied physics. 1984 Apr 15;55(8):2977-85.
3. Amami B, Addou M, Millot F, Sabioni A, Monty C. Self-diffusion in α-Fe$_2$O$_3$ natural single crystals. Ionics. 1999 Sep;5:358-70.
4. Phoon BL, Pan GT, Yang TC, Lee KM, Lai CW, Juan JC. Facile preparation of nanocrystalline TiO$_2$ thin films using electrophoretic deposition for enhancing photoelectrochemical water splitting response. Journal of Materials Science: Materials in Electronics. 2017 Nov;28:16244-53.
5. Liou YJ, Hsiao PT, Chen LC, Chu YY, Teng H. Structure and electron-conducting ability of TiO$_2$ films from electrophoretic deposition and paste-coating for dye-sensitized solar cells. The Journal of Physical Chemistry C. 2011 Dec 29;115(51):25580-9.
6. Merazga A, Al-Subai F, Albaradi AM, Badawi A, Jaber AY, Alghamdi AA. Effect of sol–gel MgO spin-coating on the performance of TiO$_2$-based dye-sensitized solar cells. Materials Science in Semiconductor Processing. 2016 Jan 1;41:114-20.
7. Lindgren T, Mwabora JM, Avendaño E, Jonsson J, Hoel A, Granqvist CG, Lindquist SE. Photoelectrochemical and optical properties of nitrogen doped titanium dioxide films prepared by reactive DC magnetron sputtering. The Journal of Physical Chemistry B. 2003 Jun 19;107(24):5709-16.
8. Parrino F, Palmisano L, editors. Titanium dioxide (TiO$_2$) and its applications. elsevier; 2020 Nov 29.
9. Chen Y, Hong L, Xue H, Han W, Wang L, Sun X, Li J. Preparation and characterization of TiO$_2$-NTs/SnO$_2$-Sb electrodes by electrodeposition. Journal of Electroanalytical Chemistry. 2010 Oct 1;648(2):119-27.
10. Cheng C, Zhang H, Ren W, Dong W, Sun Y. Three dimensional urchin-like ordered hollow TiO$_2$/ZnO nanorods structure as efficient photoelectrochemical anode. Nano Energy. 2013 Sep 1;2(5):779-86.
11. Hou Y, Li X, Zou X, Quan X, Chen G. Photoelectrocatalytic activity of a Cu$_2$O-loaded self-organized highly oriented TiO$_2$ nanotube array electrode for 4-chlorophenol degradation. Environmental science & technology. 2009 Feb 1;43(3):858-63.
12. Wang R, Bai J, Li Y, Zeng Q, Li J, Zhou B. BiVO$_4$/TiO$_2$ (N$_2$) nanotubes heterojunction photoanode for highly efficient photoelectrocatalytic applications. Nano-micro letters. 2017 Apr;9:1-9.
13. Li M, Liu H, Lv T, Ding M. Synergistic effect of the valence bond environment and exposed crystal facets of the TiO$_2$/SnS$_2$ heterojunction for achieving enhanced electrocatalytic oxygen evolution. Journal of Materials Chemistry A. 2018;6(8):3488-99.
14. Bakhshandeh F, Azarniya A, Hosseini HR, Jafari S. Are aluminium titanate-based nanostructures new photocatalytic materials? Possibilities and perspectives. Journal of Photochemistry and Photobiology A: Chemistry. 2018 Feb 15;353:316-24.
15. Trung ND, Tri N, Phuong PH, Anh HC. Synthesis of highly active heterostructured Al$_2$TiO$_5$/TiO$_2$ photocatalyst in a neutral medium. Journal of Nanomaterials. 2020;2020(1):6684791.
16. Stojadinović S, Radić N, Vasilić R. High photocatalytic activity of TiO$_2$/Al$_2$TiO$_5$ coatings obtained by plasma electrolytic oxidation of titanium. Materials Letters. 2023 May 1;338:134069.
17. Trung ND, Anh HC, Tri N, Loc LC. Fabrication of TiO$_2$/Al$_2$TiO$_5$ nanocomposite photocatalysts. International Journal of Nanotechnology. 2020;17(7-10):607-22.
18. Nguyen DT, Nguyen TH, Nguyen TN. Al$_2$TiO$_5$/SBA-15 promoting photocatalytic degradation of cinnamic acid. CTU Journal of Innovation and Sustainable Development. 2020 Jul 31;12(2):45-52.
19. Hajihashemi M, Shamanian M, Ashrafizadeh F. Band gap tuning of oxygen vacancy-induced Al$_2$O$_3$-TiO$_2$ ceramics processed by spark plasma sintering. Journal of Electroceramics. 2022 Feb 1:1-6.
20. Brinker CJ, Scherer GW. Sol-gel science: the physics and chemistry of sol-gel processing. Academic press; 2013 Oct 22.
21. Hench LL, West JK. The sol-gel process. Chemical reviews. 1990 Jan 1;90(1):33-72.
22. Klein LC, editor. Sol-gel optics: processing and applications. Springer Science & Business Media; 2013 Nov 27.
23. Yang H, Zhu M, Li Y. Sol–gel research in China: a brief history and recent research trends in synthesis of sol–gel derived materials and their applications. Journal of Sol-Gel Science and Technology. 2023 May;106(2):406-21.
24. Sobhani M, Rezaie HR, Naghizadeh R. Sol–gel synthesis of aluminum titanate (Al$_2$TiO$_5$) nano-particles. Journal of materials processing technology. 2008 Sep 12;206(1-3):282-5.
25. Andrianainarivelo M, Corriu RJ, Leclercq D, Mutin PH, Vioux A. Nonhydrolytic sol– gel process: aluminum titanate gels. Chemistry of materials. 1997 May 15;9(5):1098-102.
26. Azarniya A, Azarniya A, Hosseini HR, Simchi A. Nanostructured aluminium titanate (Al$_2$TiO$_5$) particles and nanofibers: Synthesis and mechanism of microstructural evolution. Materials Characterization. 2015 May 1;103:125-32.
27. Azarniya A, Hosseini HR. A new method for fabrication of in situ Al/Al$_3$Ti–Al$_2$O$_3$ nanocomposites based on thermal decomposition of nanostructured tialite. Journal of Alloys and Compounds. 2015 Sep 15;643:64-73.
28. Garcia-Torregrosa I, Wijten JH, Zanoni S, Oropeza FE, Hofmann JP, Hensen EJ, Weckhuysen BM. Template-free nanostructured fluorine-doped tin oxide scaffolds for photoelectrochemical water splitting. ACS applied materials & interfaces. 2019 Sep 16;11(40):36485-96.
29. Noh E, Noh KJ, Yun KS, Kim BR, Jeong HJ, Oh HJ, Jung SC, Kang WS, Kim SJ. Enhanced Water Splitting by Fe$_2$O$_3$-TiO$_2$-FTO Photoanode with Modified Energy Band Structure. The Scientific World Journal. 2013;2013(1):723201.
30. Gossen K, Ehrmann A. Influence of FTO glass cleaning on DSSC performance. Optik. 2019 Apr 1;183:253-6.
31. Zheng F, Lu H, Guo M, Zhang M. Effect of substrate pre-treatment on controllable synthesis of hexagonal WO$_3$ nanorod arrays and their electrochromic properties. CrystEngComm. 2013;15(29):5828-37.
32. Kamarulzaman NH, Salleh H, Dagang AN, Ghazali MS, Ishak N, Ahmad Z. Optimization of Titanium Dioxide Layer Fabrication Using Doctor Blade Method in Improving Efficiency of Hybrid Solar Cells. InJournal of Physics: Conference Series 2020 May 1 (Vol. 1535, No. 1, p. 012025). IOP Publishing.
33. Faddouli A, Hartiti B, Masat M, Ertugrul M, Fadili S, Labrim H. Comparative Study of Titanium Dioxide Thin Films Deposited by Spray Pyrolysis and doctor blade methodfor Solar Cells Applications. InSustainable Energy-Water-Environment Nexus in Deserts: Proceeding of the First International Conference on

Sustainable Energy-Water-Environment Nexus in Desert Climates 2022 Apr 26 (pp. 393-398). Cham: Springer International Publishing.

34. Berni A, Mennig M, Schmidt H. Doctor blade. Springer US; 2004.

35. Patterson AL. The Scherrer formula for X-ray particle size determination. Physical review. 1939 Nov 15;56(10):978.

36. López R, Gómez R. Band-gap energy estimation from diffuse reflectance measurements on sol–gel and commercial TiO_2: a comparative study. Journal of sol-gel science and technology. 2012 Jan;61:1-7.

37. Kundu A, Fisher TS. Harnessing the thermogalvanic effect of the ferro/ferricyanide redox couple in a thermally chargeable supercapacitor. Electrochimica Acta. 2018 Aug 10;281:357-69.

38. Sivula K. Metal oxide photoelectrodes for solar fuel production, surface traps, and catalysis. The journal of physical chemistry letters. 2013 May 16;4(10):1624-33.

39. Wang Z, Zhu H, Tu W, Zhu X, Yao Y, Zhou Y, Zou Z. Host/guest nanostructured photoanodes integrated with targeted enhancement strategies for photoelectrochemical water splitting. Advanced Science. 2022 Jan;9(2):2103744.

40. Scandola L, Latorrata S, Matarrese R, Cristiani C, Nova I. Effect of thickness and cracking phenomena on the photocatalytic performances of Ti/TiO_2 photoanodes produced by dip coating. Materials Chemistry and Physics. 2019 Aug 1;234:1-8.

41. Joudi F, Naceur JB, Ouertani R, Chtourou R. A novel strategy to produce compact and adherent thin films of SnO_2/TiO_2 composites suitable for water splitting and pollutant degradation. Journal of Materials Science: Materials in Electronics. 2019 Jan 15;30:167-79.

42. Zhao H, Li H, Yu H, Chang H, Quan X, Chen S. CNTs–TiO_2/Al_2O_3 composite membrane with a photocatalytic function: Fabrication and energetic performance in water treatment. Separation and Purification Technology. 2013 Sep 15;116:360-5.